Check for updates

ADVANCED ENERGY MATERIALS
www.advenergymat.de

MgB_2Se_4 Spinels (B = Sc, Y, Er, Tm) as Potential Mg-Ion Solid Electrolytes – Partial Ionic Conductivity and the Ion Migration Barrier

*Clarissa Glaser, Manuel Dillenz, Kanchan Sarkar, Mohsen Sotoudeh, Zhixuan Wei, Sylvio Indris, Ruben Maile, Marcus Rohnke, Klaus Müller-Buschbaum, Axel Groß, and Jürgen Janek**

The magnesium chalcogenide spinel $MgSc_2Se_4$ with high Mg-ion room-temperature conductivity has recently attracted interest as solid electrolyte for magnesium ion batteries. Its ionic/electronic mixed-conducting nature and the influence of the spinel composition on the conductivity and Mg^{2+} migration barrier are yet not well understood. Here, results from a combined experimental and computational study on four MgB_2Se_4 spinels (B = Sc, Y, Er, Tm) are presented. The room-temperature ionic conductivities ($\sigma_{ion} = 2 \times 10^{-5}$–$7 \times 10^{-5}$ S cm^{-1}) of the spinels are accurately measured, as electron transport is effectively suppressed by purely Mg-ion conducting electrode interlayers. Using the same approach, reversible Mg plating/stripping as well as good electrochemical stability are achieved. Driven by the good accordance of the computationally and experimentally obtained Mg^{2+} migration barriers E_a(th) and E_a, respectively, further periodic density functional calculations are performed on the MgB_2Se_4 spinel system, revealing the role of trigonal distortion on the migration path geometry and E_a(th). These findings provide deeper understanding how to reach small Mg^{2+} migration barriers E_a in the MgB_2Se_4 spinels.

1. Introduction

With the growing demand on portable and resource-saving energy storage systems, multivalent-ion-based batteries with potentially higher energy densities and lower cost than the present-day lithium-ion batteries have attracted significant interest.[1,2] Among these alternative next-generation batteries, rechargeable magnesium batteries (RMB) stand out due to the excellent characteristics of the Mg anode. Magnesium has a much lower standard reduction potential (−2.37 V vs SHE) than Zn and Al metals (−0.76 and −1.66 V) and a volumetric capacity of 3833 mAh cm^{-3} which is almost twice that of Ca and Li and three times as much as Na. Furthermore, magnesium is highly abundant in the earth's crust (with 2.1% ≈10^4 times more often than lithium) and suspected to be less prone to dendrite formation as anode, compared to lithium.[3]

To circumvent the drawbacks of liquid-based cell systems such as the passivation and corrosion of the Mg electrode, and ensure a lower susceptibility to dendrite formation as well as higher levels of safety, solid-state battery concepts are pursued.[1,4,5] Here, one of the main challenges is to develop a solid electrolyte (SE) that has a sufficient Mg-ion room-temperature conductivity

C. Glaser, Z. Wei, M. Rohnke, J. Janek
Institute of Physical Chemistry
Justus Liebig University Giessen
Heinrich-Buff-Ring 17, D-35392 Giessen, Germany
E-mail: juergen.janek@phys.chemie.uni-giessen.de

The ORCID identification number(s) for the author(s) of this article can be found under https://doi.org/10.1002/aenm.202402269

© 2024 The Authors. Advanced Energy Materials published by Wiley-VCH GmbH. This is an open access article under the terms of the Creative Commons Attribution-NonCommercial-NoDerivs License, which permits use and distribution in any medium, provided the original work is properly cited, the use is non-commercial and no modifications or adaptations are made.

DOI: 10.1002/aenm.202402269

C. Glaser, Z. Wei, M. Rohnke, J. Janek
Center for Materials Research (ZfM)
Justus Liebig University Giessen
Heinrich-Buff-Ring 16, D-35392 Giessen, Germany

M. Dillenz, K. Sarkar, M. Sotoudeh, A. Groß
Institute of Theoretical Chemistry
Ulm University
Albert-Einstein-Allee 11, D-89081 Ulm, Germany

S. Indris
Institute for Applied Materials-Energy Storage Systems (IAM-ESS)
Karlsruhe Institute of Technology (KIT)
Hermann-von-Helmholtz-Platz 1, D-76344 Eggenstein-Leopoldshafen, Germany

S. Indris
Applied Chemistry and Engineering Research Centre of Excellence (ACER CoE)
Université Mohammed VI Polytechnique (UM6P)
Lot 660, Hay Moulay Rachid, Ben Guerir 43150, Morocco

(σ_{ion} > 4–5 mS cm^{-1}).[6] The high charge density of Mg^{2+}, compared to the Li^+/Na^+ alkali counterparts, results in a much stronger Coulomb interaction in the solid host-framework, leading to typically sluggish Mg-ion mobility.[1] For this reason, the design of the crystal structure is fundamental as several structural factors can mitigate the strong Coulomb interactions experienced by the Mg^{2+} ion.[2,7] In general, materials owning interconnected 3D pathways, such as NASICON and spinel compounds, provide better platforms to support long-range ion diffusion, while 2D and 1D pathways are more easily blocked by intrinsic anti-site or extrinsic point defects. Compared to NASICON-structured compounds and other crystal structures, the spinel structure MgB_2X_4 (B = trivalent cation, X = chalcogenide) offers – apart from the 3D paths – a relatively large distance between the mobile Mg-cation in its transition state and the neighboring B-cations. This results in inherently weaker cation-cation repulsion in the activated state, possibly crucial to enabling multivalent-ion conduction even at ambient temperature.[2] In parallel, previous studies have shown that fast ion motion can be achieved when the energetically stable site of the mobile ion is less favored, in terms of coordination, than the activated site.[8] In the normal spinel structure, the Mg-ions, which typically strongly prefer the octahedral coordination environment, reside in tetrahedral sites (*tet*). During migration, the Mg-ions hop across an empty octahedral activated site (*oct*) to reach the next tetrahedral site which is expected to lead to a flattening of the energy profile along the *tet-oct-tet* migration path according to the Brønsted-Evans-Polanyi principle.[9–11]

Motivated by the features of the spinel structure, Canepa et al. studied a series of d^0-metal-based MgB_2X_4 spinels (B = Sc, Y, and In, X = S, Se, Te) by first principles-based nudged elastic band (NEB) calculations and predicted low migration barriers of E_a(th) = 0.36–0.42 eV[9] in agreement with our own corresponding computational studies.[11–13] Canepa et al. successfully synthesized $MgSc_2Se_4$ and determined a Mg^{2+} migration barrier of E_a(NMR) = 0.37 ± 0.09 eV by means of ^{25}Mg static variable-temperature spin-lattice relaxation nuclear magnetic resonance (SLR NMR) measurements, consistent with their computed data. As a first approach to determine the ionic conductivity of $MgSc_2Se_4$, they performed electrochemical impedance spectroscopy (EIS) with ion-blocking electrodes and interpreted the spectra according to the conventional model for mixed ionic-electronic conductors (MIECs) described by Jamnik and Maier.[9,14] Later on, in our previous work, we critically discussed the shortcomings of this approach in case of $MgSc_2Se_4$ and presented an alternative way, allowing accurate and unequivocal characterization of the ionic conductivity.[15] Specifically, a new kind of symmetrical transference cell is used, containing a pure Mg-ion conducting interlayer between the ion-blocking electrodes and the spinel pellet, to effectively suppress the electron transport. As a result, the partial ionic conductivity (σ_{ion} = 2.4–5.5 × 10^{-5} S cm^{-1} at room-temperature) was well determined from high-quality impedance spectra using a modified equivalent circuit, describing the impedance of a MIEC between charge carrier specific blocking electrodes and interlayers (adapted from previous works).[16–18] Furthermore, this approach, including electron-blocking interlayers, may also be an option to prevent self-discharge of a charged full cell due to the reported electronic conductivity (σ_{el} = ≈10^{-8} S cm^{-1} at room-temperature)[9,15,19] of the $MgSc_2Se_4$ SE. This self-discharge is proposed to arise from increased carrier concentration caused by point defects, and/or the presence of electron conducting secondary phases.[20,21] The latter seems to contribute to the electronic conductivity in any case, as Kundu et al. demonstrated that electronic transport occurs via a Berthelot-type mechanism of metal-type inclusions (e.g., Sc/ScSe), while Wang et al.'s attempts of compositional tuning to avoid point defects were rather unsuccessful.[19,21,22]

Recently, Koettgen et al. used density functional theory to calculate the Mg^{2+} migration barriers and the stability of several MgB_2X_4 (B = lanthanide, X = S, Se) spinels.[23] In their work, they demonstrated that the balance between a low E_a(th) and a stable spinel phase (with respect to competing AB_2X_4-type phases) is primarily given for the selenide spinels with the ionic radius r(Ln) of the lanthanides from Lu to Er [r(Lu–Er) = 0.861–0.890 Å; E_a(th,Lu–Er) = 0.369–0.358 eV]. These predicted stabilities agree well with experimental results (except for Ho).[24,25] Thus, this group of lanthanide-based selenide spinels emerges as attractive candidate for Mg-ion solid electrolytes, not least due to the predicted slightly lower migration barriers compared to the prototype $MgSc_2Se_4$. We assumed that the electrochemical and theoretical study of this series of spinels will provide a deeper understanding of their transport properties. To this end, we report here the successful synthesis of four MgB_2Se_4 spinels (B = Sc, Er, Tm, Y) together with their structural characterization by X-ray diffraction (XRD) and ^{25}Mg magic-angle spinning nuclear magnetic resonance (MAS NMR) spectroscopy. Furthermore, the partial conductivities as well as the Mg^{2+} migration barriers of the spinels with mixed ionic/electronic nature are evaluated from EIS and polarization measurements using charge carrier specific blocking electrodes and interlayers. Due to the good agreement of our experimental and computational predicted migration barriers, we extended our theoretical study based on periodic density functional theory (DFT) calculations to provide a deeper understanding on the structural details defining the migration barrier. These results are followed by further electrochemical investigations, demonstrating the good electrochemical stability and a reversible Mg plating/stripping cycling performance of the spinels. To the best of our knowledge, this is the most comprehensive report on Mg-ion conducting selenide spinels.

2. Results and Discussion

2.1. Structure Information of MgB_2Se_4 Spinels

The MgB_2Se_4 spinels (B = Er, Tm, Y) were initially prepared according to our reported one-step synthesis of $MgSc_2Se_4$[15] by reacting stoichiometric amounts of the elemental powders at 950 °C for 20 h. However, although high-purity $MgSc_2Se_4$ was obtained with this procedure, Rietveld refinement results based on the XRD patterns of the other three spinels (Figures S1 and S2, Supporting Information) reveal a significant fraction of

R. Maile, K. Müller-Buschbaum
Institute of Inorganic and Analytical Chemistry
Justus Liebig University Giessen
Heinrich-Buff-Ring 17, D-35392 Giessen, Germany

© 2024 The Authors. Advanced Energy Materials published by Wiley-VCH GmbH

16146840, 0, Downloaded from https://onlinelibrary.wiley.com/doi/10.1002/aenm.202402269 by Karlsruher Institut F., Wiley Online Library on [16/09/2024]. See the Terms and Conditions (https://onlinelibrary.wiley.com/terms-and-conditions) on Wiley Online Library for rules of use; OA articles are governed by the applicable Creative Commons License

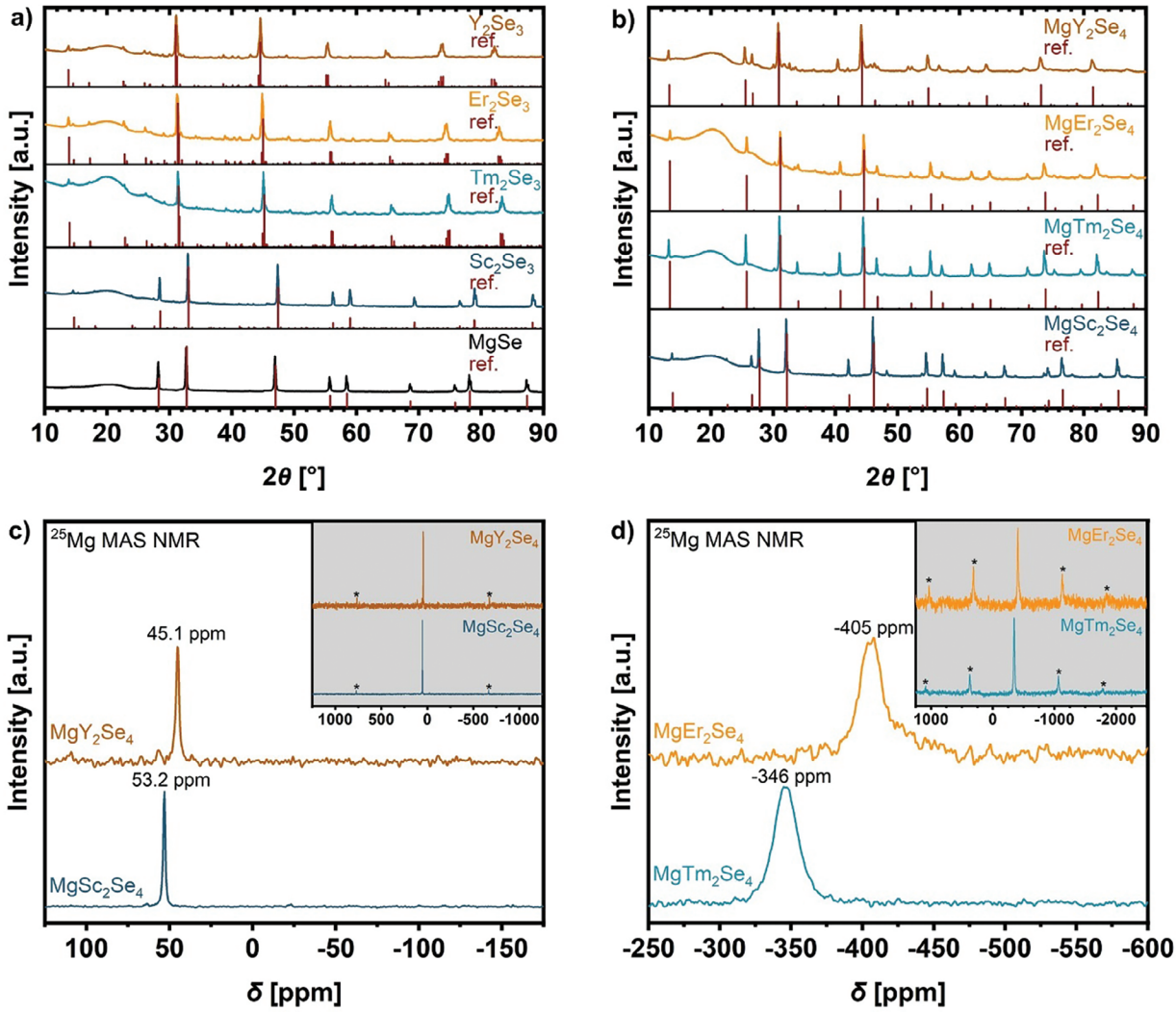

Figure 1. XRD patterns shown for a) synthesized binary selenides MgSe, Sc_2Se_3, Tm_2Se_3, Er_2Se_3 and Y_2Se_3, and b) synthesized spinels $MgSc_2Se_4$, $MgTm_2Se_4$, $MgEr_2Se_4$ and MgY_2Se_4 via the two-step route. ^{25}Mg solid-state NMR is performed for the characterization of Mg positions in c) $MgSc_2Se_4$ (one-step synthesis) and MgY_2Se_4, and d) $MgTm_2Se_4$ and $MgEr_2Se_4$. The spinning sidebands are marked with an asterisk. Data for $MgSc_2Se_4$ reproduced with permission.[15] Copyright 2023, Wiley-VCH.

impurities. The samples contained undesired B_2O_2Se between 6.2 wt% and 12.8 wt% and partially unreacted binary phases with up to 59.0 wt%, making them unusable for further analysis. As the experimental conditions for the spinel syntheses were identical, the higher content of oxide species compared to the Sc-based spinel might possibly be explained by a higher purity of the Sc powder, even if metal precursors with the same purity were purchased. To still obtain the new spinels in high purity, nevertheless, we carried out a two-step synthesis, using metal chips with less surface area and therefore probably less oxide impurity than the corresponding metal powder precursors. The XRD patterns of the first step of the synthesis (**Figure 1a**), the formation of the binary selenides, indicate B_2Se_3 compounds with a comparable high purity to Sc_2Se_3 and MgSe prepared from precursor powders. Thus, the binary selenides were found to be suitable reactants for synthesizing the corresponding spinels in a subsequent reaction step. As shown in Figure 1b, clearly fewer intensive peaks of impurities could be found in the XRD patterns of the final products using this two-step procedure, although the formation energy is much lower for the spinels built from the binaries.[9] The performed Rietveld refinements (Figure S3, Supporting Information) confirm the reduced fraction of B_2O_2Se and unreacted binaries in $MgTm_2Se_4$ (4.3 wt% and 0 wt%), $MgEr_2Se_4$ (3.0 wt% and 0.6 wt%), and MgY_2Se_4 (2.0 wt% and 8.9 wt%), as well as the spinel-type structure with Fd-3m space group (additional crystallographic data in Tables S1–S8, Supporting Information). The spinel structure consists of a cubic dense packing of Se-anions, where the B-ions reside in 16d sites (octahedra) and the Mg-ions occupying the 8a sites (tetrahedra).

To further investigate the position of the Mg-ions, ^{25}Mg MAS NMR spectroscopy was carried out. The ^{25}Mg nucleus has a nuclear spin $I = 5/2$ and a large nuclear quadrupolar moment $Q = 201$ mb[26] and thus is very sensitive to asymmetric local environments. The ^{25}Mg MAS NMR spectra (Figure 1c,d)

© 2024 The Authors. Advanced Energy Materials published by Wiley-VCH GmbH

16146840, 0, Downloaded from https://onlinelibrary.wiley.com/doi/10.1002/aenm.202402269 by Karlsruher Institut F., Wiley Online Library on [16/09/2024]. See the Terms and Conditions (https://onlinelibrary.wiley.com/terms-and-conditions) on Wiley Online Library for rules of use; OA articles are governed by the applicable Creative Commons License

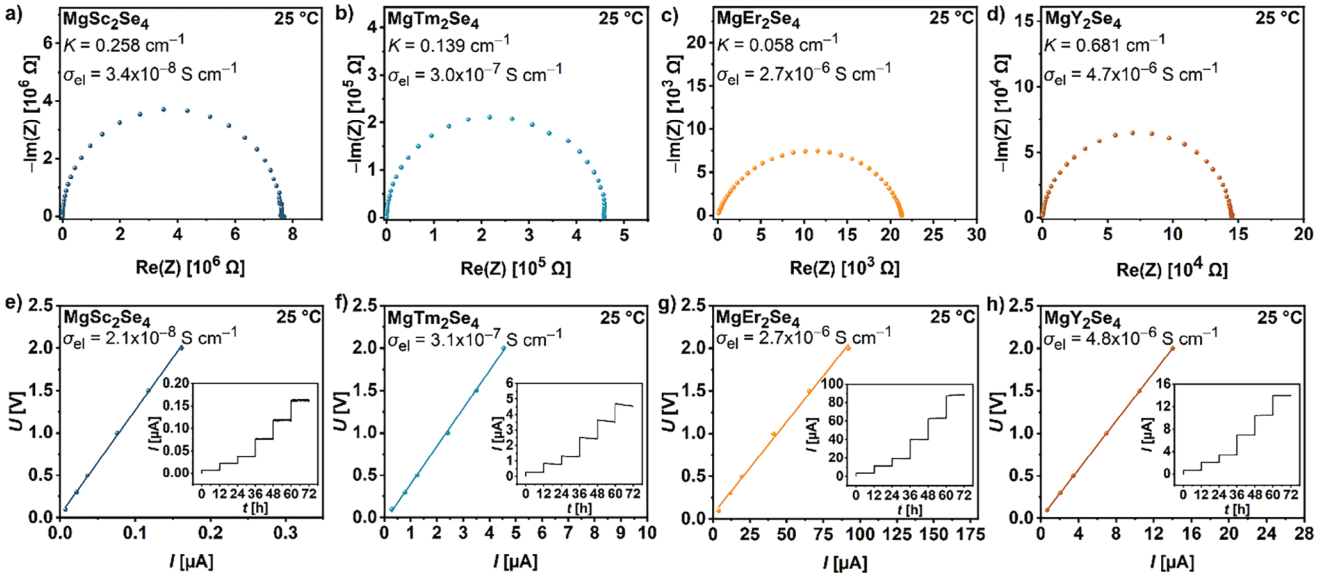

Figure 2. Nyquist plots of Au|MgB_2Se_4|Au pouch cells with a) $MgSc_2Se_4$, b) $MgTm_2Se_4$, c) $MgEr_2Se_4$ and d) MgY_2Se_4 in the frequency range from 7 MHz to 100 mHz at 25 °C; and e–h) corresponding DC polarization data obtained at different voltages (0.1 V, 0.3 V, 0.5 V, 1.0 V, 1.5 V, and 2.0 V, held for 12 h, shown in the inset) with linear fit of the ohmic electronic behavior at 25 °C. *K* represents the cell constant, as described in Equation (2). Data for $MgSc_2Se_4$ reproduced with permission.[15] Copyright 2023, Wiley-VCH.

show only a single isotropic peak for all spinels, indicating that Mg occupies exclusively the tetrahedral site. In case of the Sc- and Y-based spinels, representing diamagnetic compounds, the isotropic peak is very narrow (width of 1.5 ppm and 2.5 ppm, respectively) and the spinning sideband patterns are very weak. These characteristics reveal that the local environment, i.e., the surrounding Se tetrahedron, is highly symmetric. Instead, for the lanthanide-based spinels, consistent with their reported paramagnetism,[24] much broader isotropic peaks with large negative shifts and broader spinning sideband patterns were observed. Furthermore, energy disperse X-ray spectroscopy (EDS) images superimposed to scanning electron micrographs (SEM) display the uniform distribution of the elements Mg, Sc/Tm/Er/Y and Se in the samples. The spinel stoichiometry, which is ideally 1:2:4, is confirmed by the observed atomic ratios (Figure S4, Supporting Information), including small deficits especially in the Se fraction (0–17.5%), probably due to Se evaporation from the sample during the high-temperature synthesis. To gain more precise information about the inclusion of impurities in the nano-scale range, high-angle annular dark-field scanning transmission electron microscopy (HAADF-STEM) imaging including EDS mapping was performed (Figures S5–S8, Supporting Information). The recorded maps show a homogeneous distribution of the elements Mg, Sc/Tm/Er/Y and Se in the bulk of the particles, while some inhomogeneity can be observed at the edges, clearly visible in the layered EDS maps of the selected $MgSc_2Se_4$ and $MgEr_2Se_4$ particles but certainly also the case for $MgTm_2Se_4$ and MgY_2Se_4. This observed deviation from the spinel stoichiometry at the particle edges suggests that other phases must necessarily be present, presumably from associated elements or binary selenides. Apart from that, the collected TEM images demonstrate a typical particle size in the low micrometer range for all spinel powders ($MgSc_2Se_4$: 1–3 μm, $MgTm_2Se_4$: 0.5–1.5 μm, $MgEr_2Se_4$: 0.5–3 μm, MgY_2Se_4: 1–10 μm) (Figures S9–S12, Supporting Information), while the recorded selected area electron diffraction (SAED) patterns during the TEM measurements confirm the spinel structure as well.

2.2. Electronic Conductivity σ_{el}

To determine the room-temperature partial electronic conductivity of the MgB_2Se_4 spinels, EIS and chronoamperometry (CA) measurements were performed. Following the investigation of $MgSc_2Se_4$ in our earlier work,[15] we assembled symmetrical Au|MgB_2Se_4|Au pouch cells, containing a spinel pellet with vapor-deposited Au layers as ion-blocking electrodes. In the Nyquist plots (**Figure** 2a–d), produced from the EIS measurements, depressed semicircles with missing low-frequency tail were observed for all samples, as already obtained for $MgSc_2Se_4$.[9,15,19] These similarities to $MgSc_2Se_4$ indicate that the three new spinels seem to be MIECs as well, which have an electronic current path in parallel with the ionic current path. As there is no blockage of the electron transport due to the Au electrodes, there is no interface capacitance, explaining the lack of the capacitive tail at very low frequencies.[16] Besides that, the electronic current is much larger than the blocked ionic current, possibly even at high frequencies where the interfacial capacitance of the ions is short-circuited. Thus, the observed semicircle is only due to the combination of the electronic resistance and the geometrical capacitance, without any relation to the ionic resistance or the interfacial capacitance. For this reason, R_{el}, denoted as electronic resistance, can be determined based on the total resistance of the semicircle and then used to calculate the electronic conductivity σ_{el} by applying Equation (2) (Experimental Section). In comparison to $MgSc_2Se_4$ ($\sigma_{el} = 3.4 \times 10^{-8}$ S cm^{-1}), up to two orders of magnitude higher electronic conductivity for the new MgB_2Se_4 spinels [$\sigma_{el}(MgTm_2Se_4) = 3.0 \times 10^{-7}$ S cm^{-1},

© 2024 The Authors. Advanced Energy Materials published by Wiley-VCH GmbH

16146840, 0, Downloaded from https://onlinelibrary.wiley.com/doi/10.1002/aenm.202402269 by Karlsruher Institut F., Wiley Online Library on [16/09/2024]. See the Terms and Conditions (https://onlinelibrary.wiley.com/terms-and-conditions) on Wiley Online Library for rules of use; OA articles are governed by the applicable Creative Commons License

$\sigma_{el}(MgEr_2Se_4)$ = 2.7 × 10^{-6} S cm^{-1}, $\sigma_{el}(MgY_2Se_4)$ = 4.7 × 10^{-6} S cm^{-1}] were calculated, although a smaller direct bandgap is predicted for $MgSc_2Se_4$ (E_B = 1.727 eV)[27] than for MgY_2Se_4 (E_B = 2.020 eV).[28] As these electronic conductivities evaluated from AC impedance data agree well with the values obtained by additional dc polarization measurements shown in Figure 2e–h, the impedance analysis is validated.

Interestingly, considering the phase composition obtained by the Rietveld refinements (Figure S3, Supporting Information), a clear trend of increasing electronic conductivity with the amount of binary impurity phases (B_2Se_3, BSe_3, etc.) emerges. While $MgSc_2Se_4$ and $MgTm_2Se_4$ contain mainly impurities of MgSe (wide-bandgap semiconductor)[29] and Tm_2O_2Se, respectively, which are probably less electron-conducting phases, the other spinels are contaminated with considerable amounts of electronically conducting Er_2Se_3 (σ_{el} = 1.3 × 10^{-1} S cm^{-1})[30] or Y_2Se_3/YSe (σ_{el} = 2.0 × 10^{-1} S cm^{-1}/3.3 × 10^{-1} S cm^{-1}).[30] This demonstrates that these impurities may have a large influence on the electronic conductivity of the investigated materials, possibly even more than point defects in the spinel phase itself, since small traces of electronically conductive impurities cannot be ruled out for all four spinels. Kundu et al.[21] suggest that these impurities may occur as nano-scaled free-electron containing inclusions around the particle surface, inducing electron transport between each other by jumping/tunneling through the low-electron conducting spinel matrix, described as a Berthelot-type conductivity.[31] This hypothesis is consistent with the inhomogeneous element distribution at the edges of the particles found in the present work, which could be attributed to electron-conducting impurity phases. Nevertheless, to make the spinels applicable, their contribution to self-discharge in electrochemical cells must be reduced either by minimizing the electronic conductivity due to optimization of the synthesis and the purity of precursors or by using electron-blocking interlayers.

2.3. Ionic Conductivity σ_{ion} and Mg^{2+} Migration Barrier E_a

For the measurements of the partial ionic conductivities and the Mg^{2+} migration barriers of the MgB_2Se_4 spinels, a sandwich-type cell configuration was used, already described for the investigation of $MgSc_2Se_4$ in our previous work.[15] Inside the cells, Mg-ion conducting and at the same time electron-blocking interlayers were inserted between the cold-pressed spinel pellet and the stainless-steel ion-blocking electrodes (SS). Hence, the interlayer does not only enable a proven better physical contact between the stiff electrodes and the rough spinel pellet,[15] but also suppresses the undesired electron transport which would otherwise make the evaluation much more difficult. As interlayer, the Mg-ion ionogel electrolyte UiO66-MgIL (σ_{el} = 1.7 × 10^{-10} S cm^{-1})[15] was used, consisting of the metal-organic framework (MOF) structure UiO-66 impregnated with an 1 M $Mg(TFSI)_2$-[EMIM][TFSI] ionic liquid (IL). **Figure 3a** shows the exemplary Nyquist plots based on room-temperature EIS measurements of the SS|UiO66-MgIL|MgB_2Se_4|UiO66-MgIL|SS cells with MgY_2Se_4 and without spinel pellet (reference cell). The Nyquist plot of the SS|UiO66-MgIL|SS reference cell exhibits only a tail, relating to an imperfect capacitor, as the expected semicircle at higher frequencies cannot be resolved due to the upper limit of the frequency range (1 MHz) of the used equipment. For this reason, a simplified equivalent circuit without constant phase element (CPE) in parallel to the resistance was chosen (see Figure 3b) to determine the ionic resistance $R1_{ion}$ of the UiO66-MgIL. Applying Equation (2), for the UiO66-MgIL-2 batch, used in this work, a room-temperature ionic conductivity σ_{ion}(UiO66-MgIL-2) = 2.8 × 10^{-4} S cm^{-1} is evaluated, slightly higher than for the UiO66-MgIL-1 batch (σ_{ion} = 9.5 × 10^{-5} S cm^{-1}) taken for the investigation of $MgSc_2Se_4$.[15] This small difference can probably be attributed to small, hardly avoidable differences in the MOF pore size or conductive salt ($Mg[TFSI]_2$) concentration. Figure 3c shows the equivalent circuit used for fitting the impedance spectra of all sandwich-type cells, where three contributions are connected in parallel: the overall (bulk and grain boundary) ionic charge transport in the spinel $R2_{ion}$, the electronic charge transport in the spinel $R2_{el}$ including the electron blockage $CPE2_{e1}$ at the UiO66-MgIL interlayer, and the geometrical capacitance $CPE2_{geo}$. This part of the model is a modification of the typical circuit used for describing the impedance of a MIEC between ion-blocking electrodes.[16–18,32] The previous circuit elements in parallel, $R1_{ion}$ and $CPE1_{ion}$, represent the UiO66-MgIL interlayers, while $CPE3_{e2}$ represents the ion-blocking stainless-steel electrodes. For the fitting, the value of $R1_{ion}$ was adjusted with Equation S1 (Supporting Information) to the thickness of the UiO66-MgIL interlayer used in each individual cell and set as a fixed resistance. A detailed overview of the accurate layer thicknesses in each cell and the obtained room-temperature resistances are listed in the Tables S9–S11 (Supporting Information). Applying Equation (2) to the fitted $R2_{ion}$, a room-temperature overall ionic conductivity of $\sigma_{ion}(MgY_2Se_4)$ = 1.4–2.6 × 10^{-5} S cm^{-1} for all three MgY_2Se_4-containg cells (shown in Figure 3a) was calculated. Since the conductivity results are almost constant for differently chosen spinel layer thicknesses [$d(MgY_2Se_4)$ = 0.72 mm, 0.86 mm, or 1.26 mm], $R2_{ion}$ is indeed primarily related to the ionic resistance of the spinel. Note that this resistance is obviously not influenced by the IL of the UiO66-MgIL interlayer, as EDS mapping of the UiO66-MgIL|$MgSc_2Se_4$|UiO66-MgIL pellet cross section after temperature dependent EIS measurements demonstrated that the IL does not penetrate into the spinel pellet.[15] As exemplary shown for the MgY_2Se_4 pellet (Figure S15, Supporting Information) in this work, this is also the case for all other used spinels pellets, which have a higher relative density ρ (see Table S10, Supporting Information) than the previous investigated $MgSc_2Se_4$ pellet (m = 160 mg, ρ = 78.6%).

Figure 3d shows exemplarily the Nyquist plots of the room-temperature EIS measurements for all spinel compounds with a pellet mass of 160 mg in the sandwich-type cells. An overview of all Nyquist plots obtained over the complete temperature range from 0 °C to 60 °C for at least three different layer thicknesses/masses per spinel are depicted in Figures S16–S19 (Supporting Information). Based on the fitted Nyquist plots the average conductivity per spinel at room-temperature and 60 °C was determined. As shown in Figure 3e, the newly examined MgB_2Se_4 spinels have a similarly high ionic conductivity as $MgSc_2Se_4$ [$\sigma_{ion}(MgSc_2Se_4)$ = 4.0 × 10^{-5} S cm^{-1}, $\sigma_{ion}(MgTm_2Se_4)$ = 6.5 × 10^{-5} S cm^{-1}, $\sigma_{ion}(MgEr_2Se_4)$ = 4.1 × 10^{-5} S cm^{-1}, $\sigma_{ion}(MgY_2Se_4)$ = 2.0 × 10^{-5} S cm^{-1} at 25 °C]. This was more or less expected due to the small differences in their predicted migration

© 2024 The Authors. Advanced Energy Materials published by Wiley-VCH GmbH

16146840, 0, Downloaded from https://onlinelibrary.wiley.com/doi/10.1002/aenm.202402269 by Karlsruher Institut F., Wiley Online Library on [16/09/2024]. See the Terms and Conditions (https://onlinelibrary.wiley.com/terms-and-conditions) on Wiley Online Library for rules of use; OA articles are governed by the applicable Creative Commons License

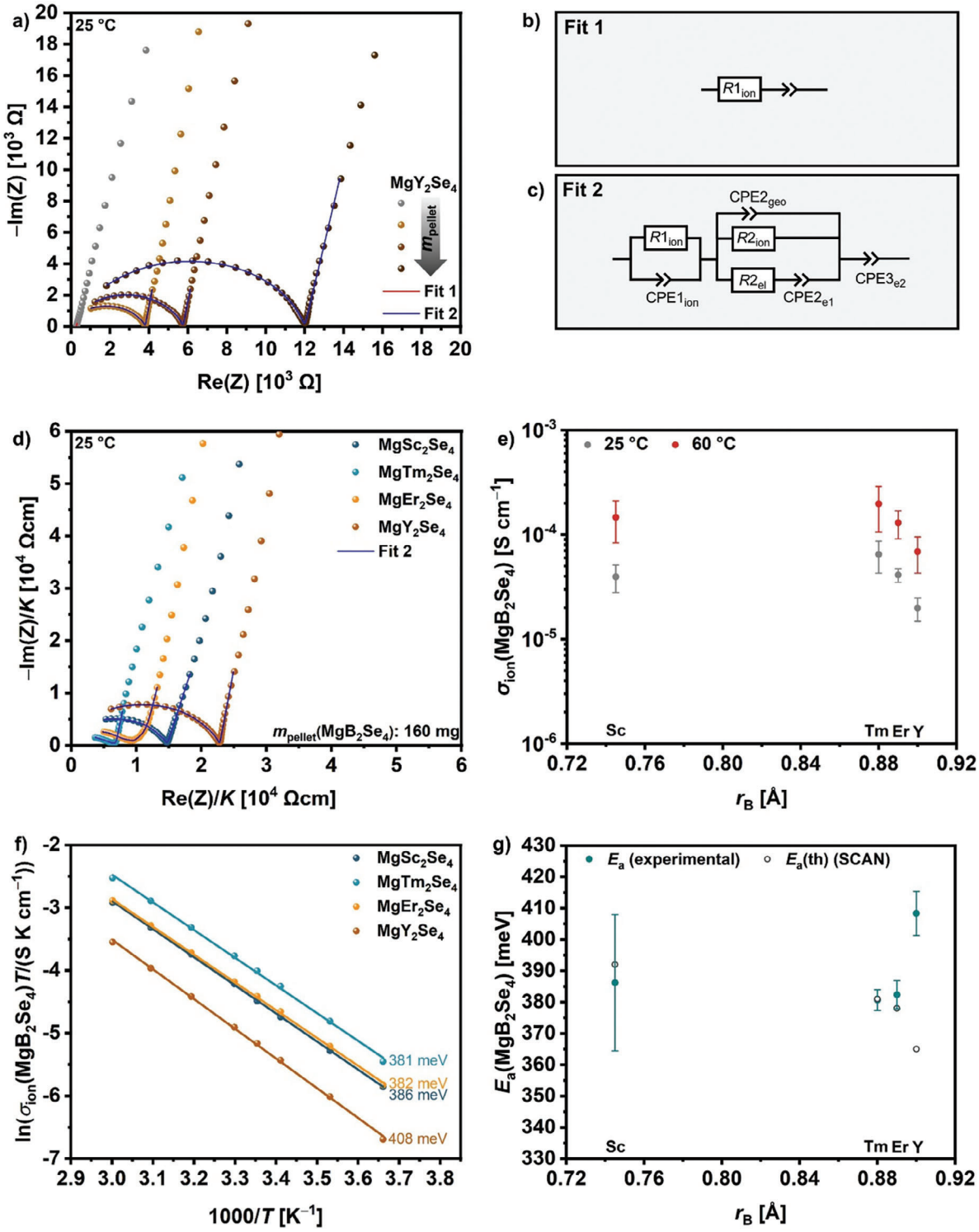

Figure 3. a) Nyquist plots of SS|UiO66-MgIL|MgB_2Se_4|UiO66-MgIL|SS cells at 25 °C exemplarily shown for MgY_2Se_4 with varied spinel pellet mass/thickness (0 mg/0 mm, 160 mg/0.72 mm, 220 mg/0.86 mm and 280 mg/1.26 mm) and used fits Fit 1 and Fit 2; applied equivalent circuit to fit the Nyquist plots for b) SS|UiO66-MgIL|SS cells (denoted as Fit 1) and c) SS|UiO66-MgIL|MgB_2Se_4|UiO66-MgIL|SS cells (denoted as Fit 2); d) comparison of Nyquist plots for SS|UiO66-MgIL|MgB_2Se_4|UiO66-MgIL|SS cells with different spinels at 25 °C exemplarily shown for a spinel pellet mass of 160 mg; e) overview of determined average ionic conductivities of the MgB_2Se_4 spinels at 25 °C and 60 °C; f) Arrhenius plots of the average ionic conductivities calculated for temperatures ranging from 0 °C to 60 °C and g) overview of determined Mg^{2+} migration barriers E_a of the MgB_2Se_4 spinels in comparison to theoretically predicted values E_a(th) by the SCAN method. Experimental data for $MgSc_2Se_4$ reproduced with permission.[15] Copyright 2023, Wiley-VCH.

© 2024 The Authors. Advanced Energy Materials published by Wiley-VCH GmbH

16146840, 0, Downloaded from https://onlinelibrary.wiley.com/doi/10.1002/aenm.202402269 by Karlsruher Institut F., Wiley Online Library on [16/09/2024]. See the Terms and Conditions (https://onlinelibrary.wiley.com/terms-and-conditions) on Wiley Online Library for rules of use; OA articles are governed by the applicable Creative Commons License

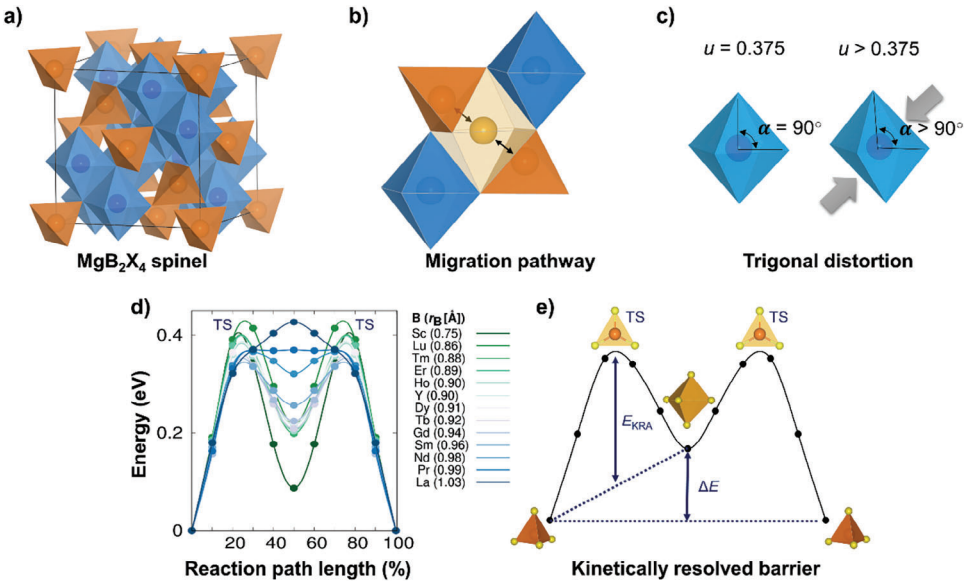

Figure 4. a) The MgB_2X_4 spinel crystal structure is shown on the left with the B-cation shown in blue and the Mg-cation in orange. b) The Mg^{2+} migration follows an interstitial mechanism. Mg^{2+} is tetrahedrally coordinated at the initial and final sites (orange) and migrates through empty octahedral (light orange) sites following a *tet-oct-tet* migration path. The transition state (TS) of the migration process is the triangular face shared by initial tetrahedral and intermediate octahedral sites. c) The trigonal distortion of octahedron specified by anion parameter u and the angle α. d) The energy along the migration path for MgB_2Se_4 spinel compounds determined by NEB. e) Schematic of the energy profile of the Mg^{2+} migration. The kinetically resolved barrier E_{KRA} and the difference in energy between tetrahedral and octahedral sites referred as site preference energy ΔE are indicated by arrows.

barriers [E_a(th) = 375–358 meV].[9,23] Note that impurities with fractions >5 wt%, in particular found in MgY_2Se_4, or the interfacial resistances that are probably material-dependent (not considered in our fittings) could have reduced the calculated conductivities. Moreover, it is worth to mention that in case of $MgEr_2Se_4$, the fitted ionic resistance of the spinel $R2_{ion}$ and the fitted total ionic resistance ($R1_{ion}$+$R2_{ion}$) are comparably higher than their corresponding estimates $R_{ion}(MgEr_2Se_4)$ and R_{ion}(SEs), directly calculated from the raw data (see Table S11, Supporting Information). In this simplified calculation, both, the total ionic resistance of the reference cell R_{ion}(UiO66-MgIL) and the sandwich-type cell R_{ion}(SEs) were directly calculated from the lowest data point at the intercept of the Re(Z) axis. From the difference of R_{ion}(SEs) and R_{ion}(UiO66-MgIL) the ionic resistance of the spinel $R_{ion}(MgEr_2Se_4)$ is given. The discrepancy between the fitted and directly calculated values results from the flattend shape of the Nyquist plots at the Re(Z) axes intercept, possibly induced due to an additional contribution from an interface or impurity. As this contribution is more integrated in the fitted values, the resistance determined directly from the raw data is lower, resulting in a slightly higher ionic conductivtiy (for example: 4.8×10^{-5} S cm^{-5} at 25 °C) for $MgEr_2Se_4$. Figure 3f shows the Arrhenius plots of the ionic conductivities for the temperature range from 0 °C to 60 °C. Applying the Arrhenius equation (Equation (3), Experimental Section), the Mg-ion migration barriers can be calculated to be $E_a(MgSc_2Se_4)$ = 386 ± 24 meV, $E_a(MgTm_2Se_4)$ = 381 ± 4 meV, $E_a(MgEr_2Se_4)$ = 382 ± 6 meV (raw data: 373 ± 5 meV), and $E_a(MgY_2Se_4)$ = 406 ± 9 meV. These values are lower than published ones for other classes of Mg-ion SEs[15] and close to our computationally derived migration barriers (E_a(th)) obtained from DFT calculations based on the strongly constrained and appropriately normed (SCAN) exchange-correlation functional (Figure 3g). In addition, our computational results exhibit a decreasing trend of the Mg^{2+} migration barrier with increasing B-ion radius r_B, in accordance to previous predictions.[9,23] This trend is not observed in the electrochemical results for the compounds synthesized here, since the experimental error exceeds the minor changes (<0.03 eV) of the migration barriers for the narrow range of the ionic radii r_B. However, to gain a deeper understanding of the calculated trend, we conducted a detailed computational study on the underlying contributions to the Mg^{2+} migration barrier, as described below.

2.4. Computational Study of Underlying Contributions to the Migration Barrier E_a(th)

Migration of Mg-ions within the spinel structure (**Figure 4a**) typically occurs via an interstitial mechanism, transitioning from initial tetrahedral sites through an empty octahedron to final tetrahedral sites (*tet-oct-tet*),[33] as illustrated in Figure 4b. The energy difference between tetrahedral and octahedral sites, known as site preference energy, influences the migration barriers, with lower barriers expected when site preference energy is minimized. However, Mg lanthanide spinels defy this trend, exhibiting lower barriers when site preference energy is maximized.[23] This phenomenon is attributed to the stabilization of the triangular transition state with increasing ionic radius r_B of the metal B. Despite its importance, the transition state energy is not usually explicitly considered in the design rule for identifying good Mg-ion conductors.

We expand upon the exploration of chemical patterns in the Mg ion transport in d^0-metal spinel chalcogenides by examining the influence of trigonal distortion (Figure 4c) on migration path

© 2024 The Authors. Advanced Energy Materials published by Wiley-VCH GmbH

16146840, 0, Downloaded from https://onlinelibrary.wiley.com/doi/10.1002/aenm.202402269 by Karlsruher Institut F., Wiley Online Library on [16/09/2024]. See the Terms and Conditions (https://onlinelibrary.wiley.com/terms-and-conditions) on Wiley Online Library for rules of use; OA articles are governed by the applicable Creative Commons License

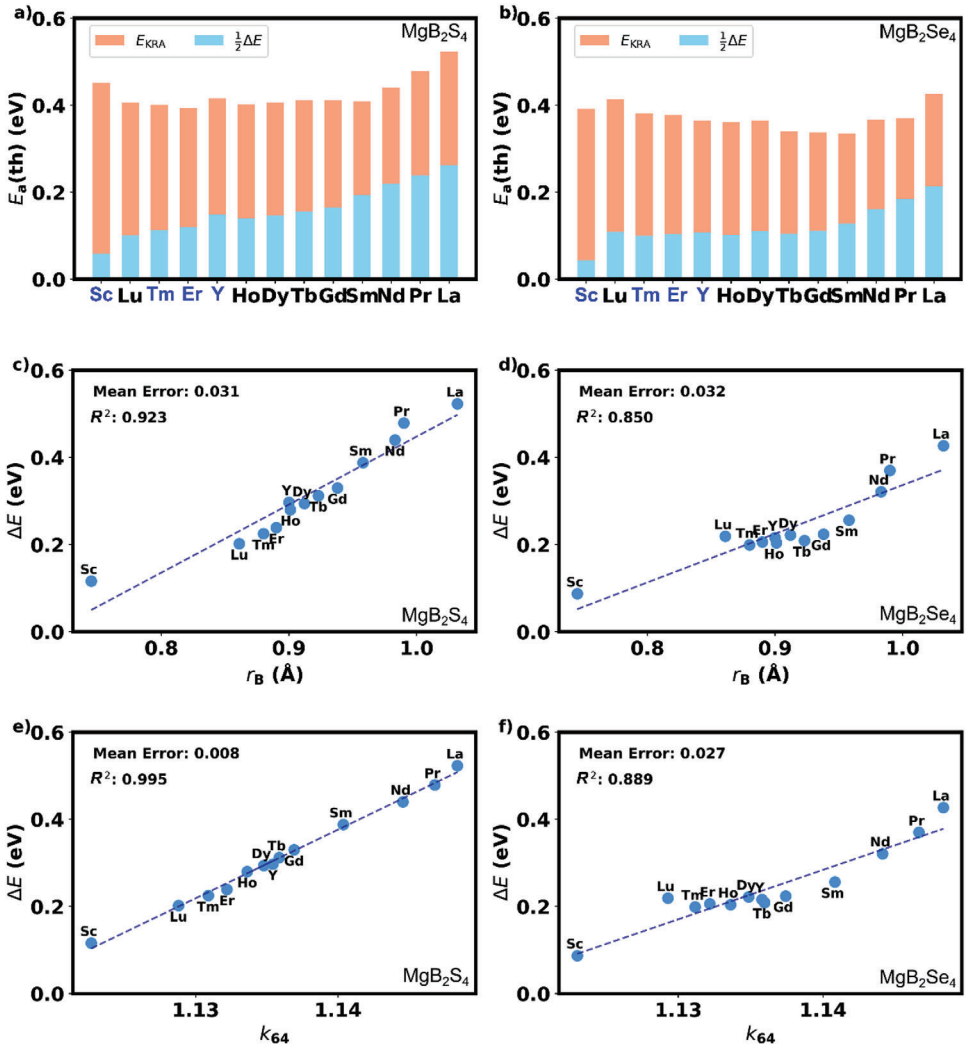

Figure 5. Migration barrier E_a(th) as the sum of half the site preference energy ΔE (blue) and the kinetically resolved barrier E_{KRA} (orange) for Mg-ion jumps in a) the MgB_2S_4 sulfide spinels and b) the MgB_2Se_4 selenide spinels. The linear regressions for ΔE as function of the ionic radius r_B of the B metal are shown with dashed lines for c) the sulfide spinels and d) the selenide spinels including the mean error and R^2 values. The linear regressions for ΔE as function of the ratio of the distance k_{64} including the mean error and R^2 values are shown for e) the sulfide spinels and f) the selenide spinels.

geometry, which corresponds to the changes in the ionic radius r_B of the metal B. Using DFT calculations combined with the NEB method, we assess migration barriers for various d^0-metal and lanthanide spinel chalcogenides (B = Sc, Y, Lu, Tm, Er, Ho, Dy, Tb, Gd, Sm, Nd, Pr, and La; X = S, Se). The calculated energy profiles along migration paths (*tet-oct-tet*) are illustrated in Figure 4d and Figure S20 (Supporting Information). We differentiate between transition state energy and site preference energy (ΔE) to determine directionally independent kinetically resolved barriers (E_{KRA}) using Equation (4) (Experimental Section), as shown in Figure 4e. While Mg-ion mobility is primarily governed by the theoretically predicted activation energy (E_a(th)), its relationship with individual contributions is complex and nonlinear. Hence, investigating the dependence of ΔE and E_{KRA} on trigonal distortion is the essence of migration barrier analysis.

The **Figure 5** provides a comprehensive analysis of the components of the migration barrier E_a(th), namely ΔE and E_{KRA}, and the correlations between ΔE and the ionic radius r_B of the transition metal B in MgB_2S_4 sulfide and MgB_2Se_4 selenide spinels. It is observed that for larger ionic radii, the site preference energy (ΔE) significantly contributes to the overall migration barrier, while for the smaller ionic radii the contribution of E_{KRA} grows and the site preference energy ΔE diminishes, as shown in Figure 5a,b. This trend is attributed to trigonal distortion resulting from the size difference between A-metal (e.g., Mg) in tetrahedral 8a sites and B-metal in octahedral 16d sites within the spinel structure. This mismatch causes a noticeable tilt in 16c and 16d octahedrons leading to an increased area in all faces of the tetrahedral site. While all faces of the tetrahedral site increase due to the distortion, only the octahedron faces shared with the tetrahedron are increasing, while others are decreasing in area. As a result, the volume of the tetrahedral 8a sites increases relative to the empty 16c sites, affecting their volume ratio as shown in Figure S21 (Supporting Information). Note that if only the

© 2024 The Authors. Advanced Energy Materials published by Wiley-VCH GmbH

16146840, 0, Downloaded from https://onlinelibrary.wiley.com/doi/10.1002/aenm.202402269 by Karlsruher Institut F., Wiley Online Library on [16/09/2024]. See the Terms and Conditions (https://onlinelibrary.wiley.com/terms-and-conditions) on Wiley Online Library for rules of use; OA articles are governed by the applicable Creative Commons License

B-metal is varied, the trigonal distortion is simply a function of r_B, explaining the linear dependence of ΔE on the ionic radius (r_B) as shown in Figure 5c,d.

Figure 5e,f illustrates the dependence of ΔE on the ratio of the bond distances k_{64} between the central cation and the Se anions in the octahedron ($d(cn_6)$) and tetrahedron ($d(cn_4)$) that was proposed to determine the site preference energy.[13] In terms of site preference energy linearity, k_{64} outperforms significantly when compared to the ionic radii (r_B), as evidenced by its superior R^2 and mean squared error. To the best of our knowledge such a relation of the ionic radius and the anion dilation parameter u was so far not derived for sulfide and selenide spinels, so that we resort to calculated bond lengths $d(cn_6)$ and $d(cn_4)$ based on DFT calculations.

A distortion free crystal is expected for $k_{64} = 1.15$ ($u = 0.375$), a value close to that of $MgLa_2Se_4$. Additionally, the trigonal distortion of d^0-metal spinels increases as r_B decreases. Consequently, the site preference energy ΔE is most significant for $MgLa_2Se_4$ and diminishes with decreasing k_{64}, as the trigonal distortion stabilizes the octahedral site compared to the tetrahedral site. This stabilization occurs through the reduction of both bond length and volume of the octahedral relative to the tetrahedral site, thereby influencing the interplay between bond length and coordination.

The continuous stabilization of the transition state with increasing r_B is rationalized by the linear dependence of E_{KRA} on the area of the triangular faces shared by tetrahedra and octahedra shown in Figure S22 (Supporting Information). This triangular face represents the bottleneck of the migration path and the transition state is found to be stabilized with increasing area of the face. Note that – since the area of the transition state is directly affected by the trigonal distortion – also a linear correlation of E_{KRA} with the ratio of distances k_{64} is observed as shown in Figure S23 (Supporting Information).

To probe the determinants of site preference energy ΔE, we examined several parameters, including the ratio of distances (k_{64}), the ionic radii of metal B (r_B) and the anion (r_X), as well as the electronegativity of B-cation (χ_B) and the anion (χ_X). Pairwise correlations are shown in a heatmap (Figure S24, Supporting Information), that reveals significant associations. Noteworthy relationships emerged between ΔE and k_{64}, as well as between ΔE and both r_B and χ_B. Additionally, correlations are apparent between k_{64} and both r_B and χ_B. These robust linear correlations hint at potential multicollinearity among parameters, which introduces complexity in estimating individual contributions to ΔE, although it aligns with chemical principles. Before proceeding further, we prioritize the evaluation of crucial parameters associated with ΔE through a comprehensive array of feature importance techniques. These methods include fitting a Random Forest model using Recursive Feature Clustering and Gini Importance,[34] as well as employing ANOVA F-value,[35] Mutual Information,[36] Permutation Importance,[37] and LASSO.[38] Consistently across these techniques, factors such as k_{64} and r_B emerge as noteworthy contributors, as highlighted by the LASSO feature importance analysis illustrated in Figure S24 (Supporting Information). Given the pairwise correlations between parameters (Figure S24, Supporting Information) and their importance in terms of feature relevance (Figure S25, Supporting Information), we directed our attention to addressing multicollinearity to streamline parameter selection for feature engineering. To this end, we evaluated multicollinearity between k_{64} and r_B using different approaches such as variance inflation factor, tolerance values, and variance proportions with a linear regression model.[39] Indeed, strong correlation between k_{64} and r_B is found suggesting the existence of a simple relation between r_B and the anion parameter u (correlating with k_{64}).

We advocate for the exploration of alternative parameters in feature engineering to predict ΔE, given the observed high correlation between k_{64} and r_B. In Figure S26 (Supporting Information), we present an optimized parameter combination for predicting ΔE, where the pairing of k_{64} and r_X proves suffice. This choice is substantiated by their non-correlated or minimally correlated nature within the current range of d^0-metal- and lanthanide-based Mg chalcogenide spinels. Additionally, k_{64} and r_X demonstrate opposite correlations with ΔE, as depicted in Figure S24 (Supporting Information). Consequently, we adopt a simple linear regression model, described by Equation (1):

$$\Delta E = -13.7164\ \text{eV} + 13.2965\ \text{eV}\ k_{64} + \left(-0.5912\ \frac{\text{eV}}{\text{Å}} r_X\right) \quad (1)$$

This model attains an optimized R^2 score of 0.95 and a mean squared error of 0.0004. Although a quadratic polynomial model could potentially enhance the R^2 score to 0.967, we prioritize the simplicity of the linear regression model. The Supporting Information includes additional graphical representations of feature importance techniques, different regression models, and advanced algorithms.

The accuracy of the simple linear relation in Figure S27 (Supporting Information) illustrates that, indeed, the site preference energy in d^0-metal- and lanthanide-based Mg chalcogenide spinels seems to predominantly depend on the influence of the trigonal distortion on the competition between bond length and coordination and thus is independent of the lattice constants. While the trigonal distortion is mostly related to the metal B and thus the ratio of distances k_{64}, also the anion affects the inherent competition between sites as evident by the contribution of the anionic radius r_X in Figure S27 (Supporting Information). In addition, the triangular transition state is affected by the increase in trigonal distortion as illustrated in Figure 4c. Here, the trigonal distortion increases the area of the transition state and thus reduces the migration barriers. Nevertheless, the here presented data set does not allow to unambiguously attribute the influence on E_{KRA} solely on the trigonal distortion independent of the lattice constants. While the site preference energy ΔE seems to predominantly dependent on the trigonal distortion and the competition between bond length and coordination, further studies on an increased chemical space that allows to decouple the effects of cell volume and trigonal distortion are required to clarify the chemical trends underlying E_{KRA}.

2.5. Electrochemical Stability and Cycling Performance

The electrochemical stability of the UiO66-MgIL ionogel electrolyte and the sandwich-type layered UiO66-MgIL|MgB_2Se_4|UiO66-MgIL pellets against Mg metal was measured via linear sweep voltammetry (LSV). For this purpose,

© 2024 The Authors. Advanced Energy Materials published by Wiley-VCH GmbH

16146840, 0, Downloaded from https://onlinelibrary.wiley.com/doi/10.1002/aenm.202402269 by Karlsruher Institut F., Wiley Online Library on [16/09/2024]. See the Terms and Conditions (https://onlinelibrary.wiley.com/terms-and-conditions) on Wiley Online Library for rules of use; OA articles are governed by the applicable Creative Commons License

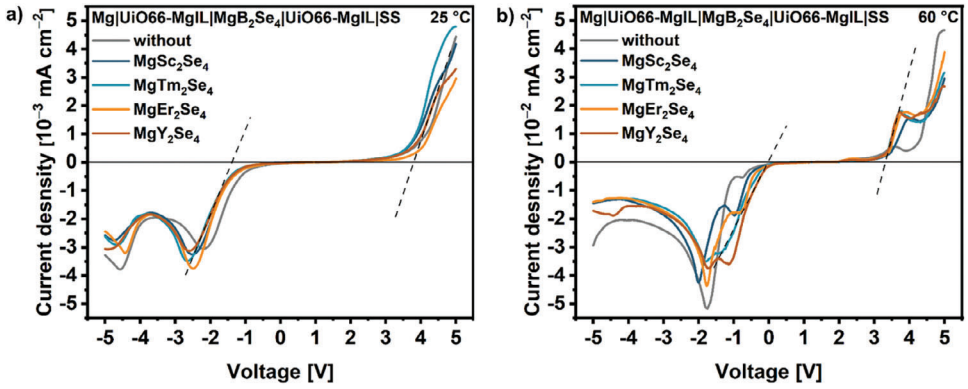

Figure 6. LSV curves of Mg|UiO66-MgIL|SS cell and Mg|UiO66-MgIL|MgB_2Se_4|UiO66-MgIL|SS two-electrode cells recorded at a scan rate of 0.1 mV s^{-1} and –0.1 mV s^{-1} at a) room-temperature and b) 60 °C with regression lines exemplarily shown for MgY_2Se_4.

asymmetric two-electrode cells were assembled using one Mg foil as both counter and reference electrode, and stainless-steel current collectors as working electrode. Note that under current load, the cell voltage does not represent the potential of the working electrode due to the overvoltage of the counter electrode. Then, starting from the open circuit voltage (OCV) the oxidation/reduction current was recorded to 5 V/−5 V (vs Mg^{2+}/Mg) with a scan rate of 0.1 mVs^{-1}/−0.1 mVs^{-1}. As shown in **Figure 6**a, at room-temperature, the oxidation current starts to grow in the range of 3.7 V to 3.9 V, while the reduction current increases significantly starting from −1.1 V to −1.3 V for all cells. Since the current profiles of the sandwich-type cells and the reference cell without spinel layer are quite identical, the UiO66-MgIL appears to limit the stability window, meaning the spinels themselves have possibly a larger range of electrochemical stability. Interestingly, all reduction current profiles show two peaks, which may be attributed to a two-step reduction of UiO66-MgIL electrolyte. A possible deposition of Mg during reduction cannot be confirmed as no Mg spots are observable on the stainless-steel electrode which is covered with adherent UiO66-MgIL (Figure S28, Supporting Information). At a temperature of 60 °C (Figure 6b), the reduction peaks merge with each other and the stability windows shrink (start oxidation: ≈3.3 V, start reduction: −0.1 V to −0.5 V), which may be correlated to a stronger decomposition of the IL or the UiO66 components, such as linkers, in the ionogel electrolyte. Apart from that, inspired by the mixed conductivity, we tested one of the spinels, $MgSc_2Se_4$, as cathode active material. However, the room-temperature galvanostatic discharge/charge voltage profiles (Figure S29, Supporting Information) recorded over ten cycles between 0.5 V and 2.7 V at 10 mA g^{-1} showed a negligibly low specific capacity. This can probably be explained by the results of the LSV at room-temperature which confirm that the spinels are not redox active between at least −1.1 V and 3.7 V and perhaps even beyond, in contrast to the report by Wang et al.[19]

In addition, we found that all MgB_2Se_4 spinels studied in this work enable reversible Mg plating and stripping at 60 °C in a symmetric Mg|UiO66-MgIL|MgB_2Se_4|UiO66-MgIL|Mg cell. As shown in **Figure 7**, the cells were initially activated by 50 cycles of alternating plating and stripping with a current density of ±1.57 μA cm^{-2} and a dwell time of 30 min per step (plated charge amount of 0.785 μAh cm^{-2}, corresponding to 2 nm of Mg per cycle assuming homogeneous plating/stripping). Afterward, the step time was increased to 10 h and further 20 cycles were recorded (15.7 μAh cm^{-2}, corresponding to 41 nm of Mg). During the cycling process stable Mg plating and stripping with a symmetrical overpotential of ≈±0.4 V was demonstrated for the cells containing the spinels with a phase purity ≥95% ($MgSc_2Se_4$, $MgTm_2Se_4$, $MgEr_2Se_4$). The performance is better and more symmetrical than for the reference cell itself (±0.5 V), possibly due to the separation of the ionogel layer in the cell by a homogenous solid-state spinel pellet. Nevertheless, note that the overpotential generally exceeds the estimated *IR* drops of 0.62 mV to 2.58 mV across the spinels, calculated from their ionic conductivities at 60 °C, indicating interface-dominating resistances inside the symmetrical cells.

Finally, to provide evidence that Mg-ion transport takes place in such sandwich-type cells, Mg plating experiments were performed in Mg|UiO66-MgIL|MgB_2Se_4|UiO66-MgIL|Cu cells using a current of –5 μA for 35 h and a temperature of 60 °C. Afterward, the surface of the Cu foil was analyzed for Mg deposits by SEM-EDS, where indeed several spots could be found. Figure S30 (Supporting Information) shows exemplarily an overview of Mg deposits with 10 μm to 30 μm in size observed for the $MgSc_2Se_4$-based cell. This Mg deposit formation confirms once again, supplementary to our first plating experiment using a Mg|MgB_2Se_4|Au cell,[15] that the here investigated Mg spinels can conduct Mg-ions.

However, although the spinels show Mg-ion conduction, reversible Mg plating/stripping cycling and an electrochemical stability till 3.7 V to be suitable in combination with the most transition metal chalcogenide cathodes,[40] their room-temperature ionic conductivity (**Figure 8**) still does not reach the order of mS cm^{-1}. In this context, it should be noted that during impedance fitting of the SS|UiO66-MgIL|MgB_2Se_4|UiO66-MgIL|SS cells, the contribution of impurities and interfacial resistances could not be extracted from the ionic resistances of the spinels. Accordingly, the actual ionic conductivity could be higher. Moreover, the spinel's potential is far from being exhausted, as some other solid electrolytes, such as Li-argyrodites, have shown that the ionic conductivity can be increased by compositional tuning.[41–45] In principle there are two main strategies: One strategy involves aliovalent substitution, which can change the concentration of the mobile ion in the compound, potentially

© 2024 The Authors. Advanced Energy Materials published by Wiley-VCH GmbH

16146840, 0, Downloaded from https://onlinelibrary.wiley.com/doi/10.1002/aenm.202402269 by Karlsruher Institut F., Wiley Online Library on [16/09/2024]. See the Terms and Conditions (https://onlinelibrary.wiley.com/terms-and-conditions) on Wiley Online Library for rules of use; OA articles are governed by the applicable Creative Commons License

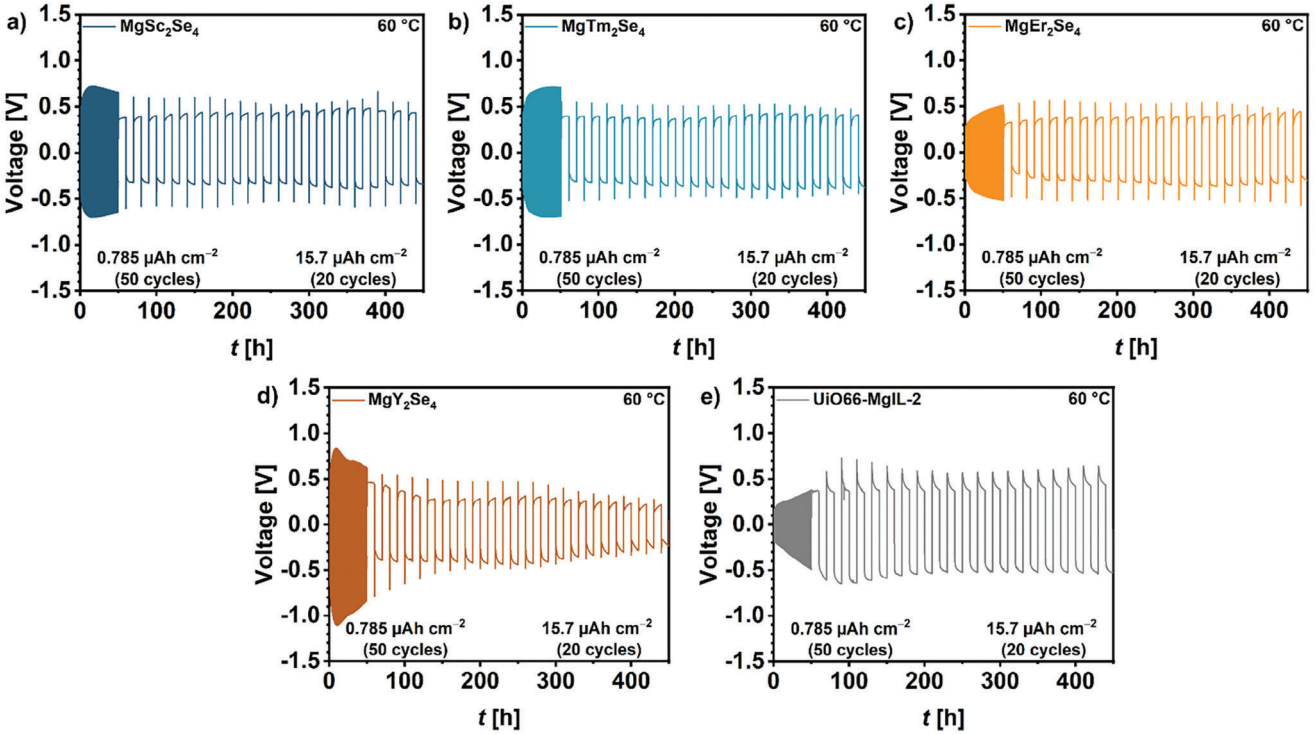

Figure 7. Long-term cycling performance during Mg plating/stripping at 60 °C for 70 cycles (50 cycles with t_{cycle} = 1 h and 20 cycles with t_{cycle} = 20 h) of Mg|UiO66-MgIL|MgB_2Se_4|UiO66-MgIL|Mg cells with a) $MgSc_2Se_4$, b) $MgTm_2Se_4$, c) $MgEr_2Se_4$, d) MgY_2Se_4, and e) without spinel pellet by applying a current density of ±1.57 µA cm^{-2}, which corresponds to a plated charge amount of 0.785 µAh cm^{-2} and 1.57 µAh cm^{-2}, respectively.

resulting in a higher ionic conductivity.[44,45] The second one is based on a high-entropy multicationic or polyanionic substitution, which increases the compositional disorder (configurational entropy) and thus the ionic conductivity.[42,43,46] Both strategies seem to be applicable for the MgB_2Se_4 spinels and should be considered in the future.

Another criterion for the application of the spinels as a SE remains their electronic conductivity. The electron transference numbers [$t_{el}(MgSc_2Se_4) = 8{\times}10^{-2}$%, $t_{el}(MgTm_2Se_4) = 5 \times 10^{-1}$%, $t_{el}(MgEr_2Se_4)$ = 6%, $t_{el}(MgY_2Se_4)$ = 19%] are more than two orders of magnitude higher than the 10^{-6}–10^{-4}% of typical SEs,[5] that increases the risk of self-discharge of a battery.[11] Here, impurities of binary compounds, such as BSe and B_2Se_3 (B = Sc, Y, Er, Tm), may play a role for the electronic transport in these materials, as we found that the electronic conductivity increases with the binary phases in the investigated spinels. Thus, there is still the potential to make the spinels applicable by minimizing the electronic conductivity due to optimization of the synthesis and the purity of precursors. Additionally, compositional tuning or the development of electron-blocking interlayers and coatings may be further options.

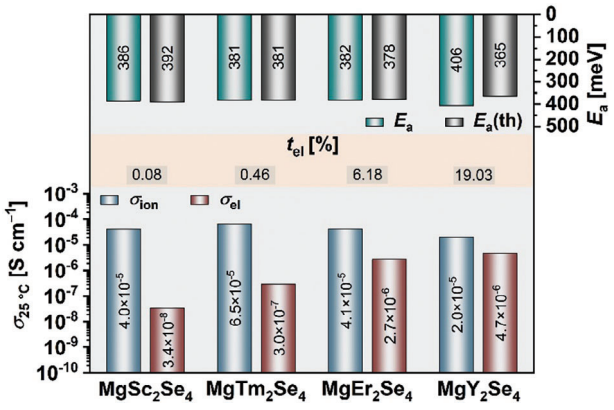

Figure 8. Overview about the room-temperature ionic conductivity σ_{ion}, the room-temperature electronic conductivity σ_{el} (from EIS), the electronic transference numbers $t_{el} = \sigma_{el}/(\sigma_{ion} + \sigma_{el})$, and the Mg^{2+} migration barrier E_a (experimental) and E_a(th) (SCAN).

3. Conclusion

In the present work, we report the successful synthesis of three MgB_2Se_4 spinels (B = Er, Tm, Y) with Fd-3m space group, showing a mixed conduction nature [$t_{el}(MgB_2Se_4) = 5 \times 10^{-1}$%–19%] like their prototype $MgSc_2Se_4$ [$t_{el}(MgSc_2Se_4) = 8 \times 10^{-2}$%]. Comparing the phase compositions obtained from Rietveld analysis with the measured electronic conductivities [$\sigma_{el}(MgSc_2Se_4) = 3.4 \times 10^{-8}$ S cm^{-1}, $\sigma_{el}(MgTm_2Se_4) = 3.0 \times 10^{-7}$ S cm^{-1}, $\sigma_{el}(MgEr_2Se_4) = 2.7 \times 10^{-6}$ S cm^{-1}, $\sigma_{el}(MgY_2Se_4) = 4.7 \times 10^{-6}$ S cm^{-1}], we suggest that impurities of binary compounds, such as BSe and B_2Se_3 (B = Sc, Y, Er, Tm), may play a role for the electronic transport in these materials. To enable an accurate determination of the ionic conductivity from impedance measurements, the electron transport was effectively blocked by introducing purely Mg-ion conducting interlayers

© 2024 The Authors. Advanced Energy Materials published by Wiley-VCH GmbH

16146840, 0, Downloaded from https://onlinelibrary.wiley.com/doi/10.1002/aenm.202402269 by Karlsruher Institut F., Wiley Online Library on [16/09/2024]. See the Terms and Conditions (https://onlinelibrary.wiley.com/terms-and-conditions) on Wiley Online Library for rules of use; OA articles are governed by the applicable Creative Commons License

in the electrochemical cells. As a result, room-temperature ionic conductivities of $\sigma_{ion}(MgTm_2Se_4) = 6.5 \times 10^{-5}$ S cm^{-1}, $\sigma_{ion}(MgEr_2Se_4) = 4.1 \times 10^{-5}$ S cm^{-1} and $\sigma_{ion}(MgY_2Se_4) = 2.0 \times 10^{-5}$ S cm^{-1} were found, partially higher than in case of $MgSc_2Se_4$ ($\sigma_{ion} = 4.0 \times 10^{-5}$ S cm^{-1}) in our previous study.[15] In addition, our further electrochemical studies demonstrate that all four spinels are electrochemically stable between −1.1 V and 3.7 V (vs Mg^{2+}/Mg), enabling reversible Mg plating/stripping and exhibiting lower Mg-ion migration barriers [$E_a(MgSc_2Se_4) = 386 \pm 24$ meV, $E_a(MgTm_2Se_4) = 381 \pm 4$ meV, $E_a(MgEr_2Se_4) = 382 \pm 6$ meV (raw data: 373 ± 5 meV) and $E_a(MgY_2Se_4) = 406 \pm 9$ meV] than other types of Mg-ion SEs. These experimentally determined Mg-ion migration barriers are in an excellent agreement with our DFT derived migration barriers E_a(th) based on the SCAN exchange-correlation functional. Moreover, the distinct influence of the trigonal distortion on the migration path geometry, and thus, the migration barrier was demonstrated. This reveals the linear correlation of the geometric descriptor based on the ratio of the bond distances in octahedral and tetrahedral sites (k_{64}) to the kinetic (E_{KRA}) and static (ΔE) contributions of the overall migration barrier E_a(th). Our results contribute to a better understanding of the transport properties in MgB_2Se_4 spinels and show their potential as SEs once an effective way to reduce the electronic conductivity is found.

4. Experimental Section

Materials: Magnesium powder (Sigma Aldrich, ≥99%), scandium powder (chemPUR, 99.9% REO), thulium powder (abcr, 99.9% REO), erbium powder (abcr, 99.9% REO), yttrium powder (abcr, 99.9% REO), thulium chips (chemPUR, 99.9% REO), erbium chips (chemPUR, 99.9% REO), yttrium chips (abcr, 99.9% REO), selenium powder (Alfa Aesar, 99.999%), gold granules (chemPUR, 99.99%), metal-organic framework ($Zr_6O_4(OH)_4(BDC)_6$, BDC = 1,4-dicarboxylate, denoted as UiO66 and prepared as),[47] magnesium bis(trifluoromethanesulfonyl)imide ($Mg(TFSI)_2$, TCI, >97%), 1-ethyl-3-methylimidazolium bis(trifluoromethanesulfonyl)imide ([EMIM][TFSI], TCI, >98%), Mg foil (chemPUR 99.98%), super P (MSE Supplies), polyvinylidene fluoride binder (HSV900 PVDF binder, ≥99.5%), glass fiber separator (GF/D, Whatman), magnesium tetrakis(hexafluoroisopropyloxy)borate ($Mg[B(hfip)_4]_2$, prepared as),[48] 1,2-dimethoxyethane (Sigma Aldrich, 99.5%), magnesium foil (Sigma Aldrich, 100 µm, 99.9%), copper foil (MSE, 9 µm, ≥99.9%).

Synthesis of MgB_2Se_4 Spinels: In the one-step synthesis, magnesium powder, scandium/thulium/erbium/yttrium powder and selenium powder were hand-milled in a molar ratio of 1:2:4 for 15 min. Then, 0.5 g of each powder mixture was pressed into a pellet (Ø = 10 mm) under a pressure of 300 MPa for 30 min. After pressing, each pellet was wrapped into a platinum foil and vacuum sealed in a separate quartz glass ampule, prior backed out at 800 °C under dynamic vacuum to remove moisture. To perform the solid-state reaction, the ampules were heated at 950 °C for 20 h (180 °C h^{-1} heating rate) in a furnace (Nabertherm with controller P 300). When the samples reached room-temperature again, the pellets were collected by breaking the ampules and afterward ground to powders.

In the two-step synthesis, first the binary selenides were prepared. MgSe and Sc_2Se_3 were synthesized from stoichiometric amounts of the elemental powders according to the previous one-step synthesis at 750 °C for 24 h (180 °C h^{-1} heating rate) and 800 °C for 30 h (60 °C h^{-1} heating rate), respectively. Instead, the Tm_2Se_3, Er_2Se_3 and Y_2Se_3 syntheses were carried out with stoichiometric amounts of selenium powder and thulium, erbium or yttrium metal chips, respectively, which were less prone against oxidation than powders. The selenium powder was placed on the bottom of a graphite crucible and then covered with the metal chips. After sealing the crucible in an evacuated quartz glass ampule, heating at 800 °C for 48 h (60 °C h^{-1} heating rate) was performed. In the second synthesis step, MgSe was mixed and pelletized in a 1:1 ratio with either Sc_2Se_3, Tm_2Se_3, Er_2Se_3 or Y_2Se_3 to obtain the corresponding MgB_2Se_4 spinel by thermal conversion. For the $MgSc_2Se_4$ synthesis the same conditions as described in the one-step synthesis were applied, while a longer heating time of 30 h was used for the other spinels. All preparations and sample treatments were performed under argon atmosphere or in vacuum.

X-Ray Diffraction (XRD): The powder XRD) patterns of the binary and ternary selenides were collected by the means of an Empyrean powder diffractometer (Malvern PANalytical Ltd) with Cu K_α radiation. To avoid contact with air and humidity, the samples placed on top of silicon zero background holders were sealed with Kapton polyimide film inside a glove box. Data were recorded in the 2θ range from 10° to 90° with a step size of 0.026° and a counting time per step of 200 s. References were taken from ICSD Inorganic Crystal Structure Database: MgSe (ICSD 53 946), Sc_2Se_3 (ICSD 651 804), $MgSc_2Se_4$ (ICSD 642 814), Tm_2Se_3 (ICSD 652 078), $MgTm_2Se_4$ (ICSD 76 051), Er_2Se_3 (ICSD 79 227), Er_2O_2Se (ICSD 25 810), $MgEr_2Se_4$ (ICSD 630 754), Y_2Se_3 (ICSD 652 183), YSe (ICSD 183 015), and MgY_2Se_4 (ICSD 76 052). Reference data retrieved from the Materials Project from database version *v2022.10.28*:[49] Tm_2O_2Se, (mp-753920) and Y_2O_2Se (mp-752658).

Rietveld Analysis: Rietveld refinements based on the powder XRD patterns were performed using the software FullProf Suite version January 2021. Start models for the Rietveld refinement were taken from references listed in Experimental Section under X-ray diffraction.

Scanning Electron Microscopy (SEM) and Energy-Dispersive X-Ray Spectroscopy (EDS): SEM images and EDS maps of the samples were obtained with a Gemini SEM 560 high-resolution scanning electron microscope (Carl Zeiss AG, Germany) at an acceleration voltage of 10 kV (pellet cross section, Cu and SS electrode) or 15 kV (SE powders). A working distance between 8 mm and 9 mm and an aperture size of 60 µm and 120 µm were chosen. All images were collected with the in-lens detector and the mapping was carried out by using an X-Max50 detector (Oxford Instruments, UK). To avoid air contamination, the samples were transferred from the glove box with a Leica EM VCT500 (Leica Microsystems Germany) shuttle.

Transmission Electron Microscopy (TEM): TEM images and EDS maps were taken by Themis 300 (Thermo Fisher Scientific) using an accelerating voltage of 300 kV. The spinel powders were dispersed on the Mo TEM grid for TEM observation. SAED patterns were collected to identify the crystal structure of the synthesized materials.

Nuclear Magnetic Resonance (NMR) Spectroscopy: ^{25}Mg MAS NMR spectroscopy was performed at a magnetic field of 11.7 T corresponding to a resonance frequency of 30.6 MHz. The measurements were carried out in 1.3 mm rotors at a spinning speed of 22 kHz with a rotor-synchronized Hahn-echo pulse sequence and a $\pi/2$ pulse duration of 3.7 µs. The recycle delay was 15 s for $MgSc_2Se_4$/MgY_2Se_4 and 1 s for $MgEr_2Se_4$/$MgTm_2Se_4$. The spectra were referenced to an aqueous solution of 5 M $MgCl_2$.

Cell Assembly and Electrochemical Measurements: The electrochemical measurements were performed with a VMP300 electrochemical workstation from Bio-Logic Science Instruments SAS and recorded with the corresponding software EC-Lab, unless specified otherwise. RelaxIS 3 software (RHD Instruments, Darmstadt, Germany) was used for fitting of the experimental EIS data.

The electronic conductivity of the MgB_2Se_4 powders was measured using pouch cells. Pellets of 6 mm to 10 mm diameter were pressed from 150 mg to 300 mg MgB_2Se_4 powder under isostatic pressure of 3000 bar for 30 min. Afterward, each pellet was separately sealed in a quartz glass ampule and sintered at 950 °C for 6 h (180 °C h^{-1} heating rate). Then, the sintered pellets were polished down to grit 4000 using SiC sandpaper. Au electrodes (Ø = 5.5–9 mm) with a thickness of 300 nm were vapor-deposited on both sides of the pellet by the mean of a sputter coater (tectra GmbH, Germany). The Au deposition rate was set to 0.15–0.2 nm s^{-1} at a pressure <10^{-6} mbar. After a second sintering step at 500 °C for 6 h, the pellets were sealed under argon into pouch cells, connected with the Au electrodes to Ni current collectors. EIS and CA measurements of the symmetrical Au|MgB_2Se_4|Au cells were performed in climate chambers

© 2024 The Authors. Advanced Energy Materials published by Wiley-VCH GmbH

16146840, 0, Downloaded from https://onlinelibrary.wiley.com/doi/10.1002/aenm.202402269 by Karlsruher Institut F., Wiley Online Library on [16/09/2024]. See the Terms and Conditions (https://onlinelibrary.wiley.com/terms-and-conditions) on Wiley Online Library for rules of use; OA articles are governed by the applicable Creative Commons License

(Weisstechnik, Germany) at 25 °C. The impedance data were collected from 7 MHz to 100 mHz with an alternating current (AC) amplitude of 10 mV. The dc polarization was carried out in six steps from 0.1 V to 2.0 V with 12 h resting time per step. From the obtained resistances R, the electronic conductivities σ_{el} were calculated based on the following equation:

$$\sigma = \frac{d}{A}\,\frac{1}{R} = \frac{K}{R} \tag{2}$$

d and A represent the thickness and the contact area of the electrolyte pellet, respectively, and are summarized in the cell constant K.

To measure the ionic conductivity, a home-made battery cell casing was used, as introduced in an earlier work.[50] Different amounts (160 mg, 220 mg and 280 mg) of MgB_2Se_4 powder were filled in the PEEK housing of the cell with a diameter of 10 mm. Then, the powders were pressed between two stainless-steel stamps (SS) at 3 t for 3 min to create a pellet inside the housing. Two purely Mg-ion conducting interlayer were added by pressing 40 mg of an ionogel SE, denoted as UiO66-MgIL, on both sides of the MgB_2Se_4 pellet under previous conditions. The ionogel SE consisted out of a Mg-ion conducting metal-organic framework (MOF) structure UiO-66 impregnated in a mass ratio of 1:1.25 with a 1 M $Mg(TFSI)_2$ ionic liquid based on [EMIM][TFSI], as described in an earlier report.[15] A constant pressure was applied by the means of the screw of aluminum framework around the homemade cell casing with 10 Nm torque. The impedance spectra of the SS|UiO66-MgIL|MgB_2Se_4|UiO66-MgIL|SS cells were recorded between 0 °C and 60 °C in a frequency range from 3 MHz to 100 mHz with an AC amplitude of 10 mV. After evaluation of the ionic resistances of the MgB_2Se_4 spinels, the ionic conductivities were calculated according to Equation (2). Then, the Mg-ion migration barriers (E_a) were obtained by rearrangement of the Arrhenius equation (Equation (3)):

$$\sigma_{ion} = \frac{\sigma_0}{T}\exp\left(-\frac{E_a}{k_B T}\right) \tag{3}$$

with σ_0 representing the conductivity prefactor.

The LSV measurements were performed with Mg|UiO66-MgIL|MgB_2Se_4|UiO66-MgIL|SS cells, which were initially assembled analogous to the cells used to determine the ionic conductivity using 220 mg MgB_2Se_4 powder (or 0 mg for reference cell) and 40 mg UiO66-MgIL per layer. Then, a polished Mg foil (Ø = 9 mm) was placed between one UiO66-MgIL layer and the SS stamp. After pressing the cell at 3 t for 1 min, LSV from open circuit voltage (OCV) to 5 V or –5 V, respectively, was carried out with a scan rate of 0.1 mV s^{-1}/–0.1 mV s^{-1} at 25 °C and 60 °C.

For the Mg plating/stripping measurements, symmetrical Mg|UiO66-MgIL|MgB_2Se_4|UiO66-MgIL|Mg cells with two Mg electrodes were prepared according to the previous procedure. Then, CP was performed over 70 cycles (50 cycles with t_{cycle} = 1 h and 20 cycles with t_{cycle} = 20 h) at 60 °C by applying a current density of 1.57 µA cm^{-2}. In case of the Mg plating experiments, Mg|UiO66-MgIL|MgB_2Se_4|UiO66-MgIL|Cu cells were assembled by using a Mg foil and a Cu foil electrode. After that CP measurements with a current of –5 µA for 35 h were carried out at 60 °C, whereby 79 µg Mg should be theoretically deposited on the Cu electrode.

To investigate $MgSc_2Se_4$ as a cathode active material, two-electrode Swagelok cells were assembled. The cathode electrode was prepared by casting 70 wt% $MgSc_2Se_4$, 20 wt% super P, and 10 wt% PVDF binder onto an Al foil, resulting in a loading mass of 1 mg cm^{-2} to 1.5 mg cm^{-2} active material. The anode, consisting of a polished Mg foil (Ø = 9 mm), was separated from the cathode by a glass fiber separator and 100 µL of a $Mg[B(hfip)_4]_2$ liquid electrolyte (0.4 M in 1,2-dimethoxyethane) was used. Galvanostatic discharge/charge voltage profiles were recorded with a Maccor Series 4000 (Maccor, USA) at room-temperature over ten cycles between 0.5 V and 2.7 V (vs Mg^{2+}/Mg) at a current density of 10 mA g^{-1}.

Computational Details: The influence of the trigonal distortion on the Mg^{2+} migration barriers was studied by periodic first-principles calculations based on DFT.[51] The projector augmented-wave method (PAW)[52] and the SCAN[53] exchange and correlation functional was used as implemented in Vienna Ab initio Simulation Package (VASP).[54] The conventional unit cell containing eight formula units with 56 atoms was chosen assuring a minimal distance of 10 Å between mobile defects. The supercell was relaxed without any restrictions until all forces on the atoms converged below 0.01 eV $Å^{-1}$. The cutoff energy was set to 520 eV and a 2 × 2 × 2 k-point mesh was used in conjunction with a convergence criterion for the total energies of 1×10^{-5} eV per supercell. The Mg-ion migration barriers were determined by the climbing image nudged elastic band (CI-NEB) method[55] using four distinct images between the initial tetrahedral and intermediate octahedral site, and the complete energy profile was obtained by mirroring at the intermediate of the migration event. The force convergence criterion for the NEB calculations was set to 0.05 eV $Å^{-1}$. All migration barriers were determined in the low-vacancy limit and upon fixing the volume to the one of the pristine structures.

In addition, possible influence of the structural distortions due to the presence of the vacancy and due to the charge compensation were checked for all experimentally synthesized compounds and are shown in Table S12 (Supporting Information).

To obtain further insight into the chemical trends for the migration barrier E_a(th), it was beneficial to separate contributions from the transition state energy E_{TS} and the site preference energy ΔE to the overall barrier E_a(th). This could be achieved by constructing directionally independent kinetically resolved activation barriers E_{KRA} (Equation (4)):

$$E_{KRA} = E_{TS} - \frac{1}{2}\left(E_{oct} - E_{tet}\right) \tag{4}$$

Note that this construction was only valid if the transition state was at 50% migration path length and breaks down if the intermediate octahedral site was the transition state of the Mg-ion migration.

Supporting Information

Supporting Information is available from the Wiley Online Library or from the author.

Acknowledgements

This work contributes to the research performed at CELEST (Center for Electrochemical Energy Storage Ulm-Karlsruhe) and was funded by the German Research Foundation (DFG) under Project ID 390874152 (POLiS Cluster of Excellence). The authors would like to thank Zhirong Zhao-Karger (KIT/Helmholtz Institute Ulm) for providing the $Mg[B(hfip)_4]_2$ salt, Yushu Tang (KIT) for the TEM measurements and Anika Siebert (JLU) for helping with the plating experiment.

Conflict of Interest

The authors declare no conflict of interest.

Data Availability Statement

The data that support the findings of this study are openly available in Zenodo at https://doi.org/10.5281/zenodo.12732117, reference number 12732117. All electronic structure calculations used in this work are made available under the Creative Commons Attribution license (CC BY 4.0) on the NOMAD repository (https://nomad-lab.eu) under the following link: https://doi.org/10.17172/NOMAD/2021.11.18-1.

Keywords

density functional theory, magnesium batteries, magnesium chalcogenide spinels, magnesium electrolytes, solid electrolytes

© 2024 The Authors. Advanced Energy Materials published by Wiley-VCH GmbH

16146840, 0, Downloaded from https://onlinelibrary.wiley.com/doi/10.1002/aenm.202402269 by Karlsruher Institut F., Wiley Online Library on [16/09/2024]. See the Terms and Conditions (https://onlinelibrary.wiley.com/terms-and-conditions) on Wiley Online Library for rules of use; OA articles are governed by the applicable Creative Commons License

Received: May 26, 2024
Revised: August 5, 2024
Published online:

[1] Y. Zhan, W. Zhang, B. Lei, H. Liu, W. Li, *Front. Chem.* **2020**, *8*, 125.
[2] Z. W. B. Iton, K. A. See, *Chem. Mater.* **2022**, *34*, 881.
[3] a) M. Guo, C. Yuan, T. Zhang, X. Yu, *Small* **2022**, *18*, 2106981; b) Y. Liang, H. Dong, D. Aurbach, Y. Yao, *Nat. Energy* **2020**, *5*, 646.
[4] P. W. Jaschin, Y. Gao, Y. Li, S.-H. Bo, *J. Mater. Chem. A* **2020**, *8*, 2875.
[5] Y. Gao, T. P. Mishra, S.-H. Bo, G. Sai Gautam, P. Canepa, *Annu. Rev. Mater. Res.* **2022**, *52*, 129.
[6] J. Janek, W. G. Zeier, *Nat. Energy* **2023**, *8*, 230.
[7] M. Dillenz, M. Sotoudeh, H. Euchner, A. Groß, *Front. Energy Res.* **2020**, *8*, 584654.
[8] a) Z. Rong, R. Malik, P. Canepa, G. Sai Gautam, M. Liu, A. Jain, K. Persson, G. Ceder, *Chem. Mater.* **2015**, *27*, 6016; b) M. Liu, Z. Rong, R. Malik, P. Canepa, A. Jain, G. Ceder, K. A. Persson, *Energy Environ. Sci.* **2015**, *8*, 964.
[9] P. Canepa, S.-H. Bo, G. Sai Gautam, B. Key, W. D. Richards, T. Shi, Y. Tian, Y. Wang, J. Li, G. Ceder, *Nat. Commun.* **2017**, *8*, 1759.
[10] a) M. G. Evans, M. Polanyi, *Trans. Faraday Soc.* **1938**, *34*, 11; b) J. N. Bronsted, *Chem. Rev.* **1928**, *5*, 231.
[11] M. Dillenz, M. Sotoudeh, C. Glaser, J. Janek, A. Groß, H. Euchner, *Batteries Supercaps* **2022**, *5*, 202200164.
[12] a) M. Sotoudeh, A. Groß, *JACS Au* **2022**, *2*, 463; b) M. Sotoudeh, A. Groß, *J. Phys. Chem. Lett.* **2022**, *13*, 10092.
[13] M. Sotoudeh, M. Dillenz, A. Groß, *Adv. Energy and Sustainable Res.* **2021**, *2*, 2100113.
[14] a) J. Jamnik, J. Maier, *J. Electrochem. Soc.* **1999**, *146*, 4183; b) J. Jamnik, J. Maier, *Phys. Chem. Chem. Phys.* **2001**, *3*, 1668.
[15] C. Glaser, Z. Wei, S. Indris, P. Klement, S. Chatterjee, H. Ehrenberg, Z. Zhao-Karger, M. Rohnke, J. Janek, *Adv. Energy Mater.* **2023**, *13*, 2301980.
[16] R. A. Huggins, *Ionics* **2002**, *8*, 300.
[17] J. Zahnow, T. Bernges, A. Wagner, N. Bohn, J. R. Binder, W. G. Zeier, M. T. Elm, J. Janek, *ACS Appl. Energy Mater.* **2021**, *4*, 1335.
[18] S. Burkhardt, M. S. Friedrich, J. K. Eckhardt, A. C. Wagner, N. Bohn, J. R. Binder, L. Chen, M. T. Elm, J. Janek, P. J. Klar, *ACS Energy Lett.* **2019**, *4*, 2117.
[19] L.-P. Wang, Z. Zhao-Karger, F. Klein, J. Chable, T. Braun, A. R. Schür, C.-R. Wang, Y.-G. Guo, M. Fichtner, *ChemSusChem* **2019**, *12*, 2286.
[20] P. Canepa, G. Sai Gautam, D. Broberg, S.-H. Bo, G. Ceder, *Chem. Mater.* **2017**, *29*, 9657.
[21] S. Kundu, N. Solomatin, Y. Kauffmann, A. Kraytsberg, Y. Ein-Eli, *Appl. Mater. Today* **2021**, *23*, 100998.
[22] S. Kundu, N. Solomatin, A. Kraytsberg, Y. Ein-Eli, *Energy Technol.* **2022**, *10*, 2200896.
[23] J. Koettgen, C. J. Bartel, G. Ceder, *Chem. Commun.* **2020**, *56*, 1952.
[24] D. Reig-i-Plessis, A. Cote, S. van Geldern, R. D. Mayrhofer, A. A. Aczel, G. J. MacDougall, *Phys. Rev. Mater.* **2019**, *3*, 114408.
[25] a) D. Reig-i-Plessis, S. V. Geldern, A. A. Aczel, D. Kochkov, B. K. Clark, G. J. MacDougall, *Phys. Rev. B* **2019**, *99*, 134438; b) J. Flahaut, M. Guittard, M. Patrie, M. P. Pardo, S. M. Golabi, L. Domange, *Acta Crystallogr.* **1965**, *19*, 14; c) M. Guittard, C. Souleau, H. Farsam, *C. R. Hebd. Acad. Sci.* **1964**, *259*, 2847.
[26] P. Raghavan, *At. Data Nucl. Data Tables* **1989**, *42*, 189.
[27] W. Tahir, G. M. Mustafa, N. A. Noor, S. M. Alay-e-Abbas, Q. Mahmood, A. Laref, *Ceram. Int.* **2020**, *46*, 26637.
[28] M. Zanib, N. A. Noor, M. A. Iqbal, I. Mahmood, A. Mahmood, S. M. Ramay, N. Y. Al-Garadi, T. Uzzaman, *Curr. Appl. Phys.* **2020**, *20*, 1097.
[29] D. J. Chadi, *Phys. Rev. Lett.* **1994**, *72*, 534.
[30] H. Bergmann, H. Hein, P. Kuhn, U. Vetter, G. Czack, E. Koch, E. Warkentin, *Sc, Y, La-Lu Rare Earth Elements C 9*, Springer Berlin Heidelberg, Berlin Heidelberg **1985**.
[31] a) B. Fisher, K. Chashka, L. Patlagan, G. Reisner, *Phys. Rev. B* **2004**, *70*, 205109; b) C. M. Hurd, *J. Phys. C: Solid State Phys.* **1985**, *18*, 6487; c) I. Balberg, *J. Appl. Phys.* **2011**, *110*, 61301.
[32] J. Maier, *Z. Phys. Chem.* **1984**, *140*, 191.
[33] M. Sotoudeh, S. Baumgart, M. Dillenz, J. Döhn, K. Forster-Tonigold, K. Helmbrecht, D. Stottmeister, A. Groß, *Adv. Energy Mater.* **2024**, *14*, 2302550.
[34] a) L. Breiman, *Mach. Learn.* **2001**, *45*, 5; b) P. Geurts, D. Ernst, L. Wehenkel, *Mach. Learn.* **2006**, *63*, 3.
[35] I. Guyon, A. Elisseef, *J. Mach. Learn. Res.* **2003**, *3*, 1157.
[36] B. C. Ross, *PLoS One* **2014**, *9*, 87357.
[37] A. Fisher, C. Rudin, F. Dominici, *J. Mach. Learn. Res.* **2019**, *20*, 1.
[38] R. Tibshirani, *J. R. Stat. Soc. Ser. B Stat. Method.* **1996**, *58*, 267.
[39] D. A. Belsley, E. Kuh, R. E. Welsch, *Regression Diagnostics. Identifying Influential Data and Sources of Collinearity*, John Wiley & Sons Inc, Hoboken, New Jersey, **1980**.
[40] C. Pei, F. Xiong, Y. Yin, Z. Liu, H. Tang, R. Sun, Q. An, L. Mai, *Small* **2021**, *17*, 2004108.
[41] X. Bai, Y. Duan, W. Zhuang, R. Yang, J. Wang, *J. Mater. Chem. A* **2020**, *8*, 25663.
[42] J. Lin, G. Cherkashinin, M. Schäfer, G. Melinte, S. Indris, A. Kondrakov, J. Janek, T. Brezesinski, F. Strauss, *ACS Mater. Lett.* **2022**, *4*, 2187.
[43] F. Strauss, J. Lin, M. Duffiet, K. Wang, T. Zinkevich, A.-L. Hansen, S. Indris, T. Brezesinski, *ACS Mater. Lett.* **2022**, *4*, 418.
[44] P. Adeli, J. D. Bazak, A. Huq, G. R. Goward, L. F. Nazar, *Chem. Mater.* **2021**, *33*, 146.
[45] L. Zhou, N. Minafra, W. G. Zeier, L. F. Nazar, *Acc. Chem. Res.* **2021**, *54*, 2717.
[46] Y. Zeng, B. Ouyang, J. Liu, Y.-W. Byeon, Z. Cai, L. J. Miara, Y. Wang, G. Ceder, *Science* **2022**, *378*, 1320.
[47] Z. Wei, R. Maile, L. M. Riegger, M. Rohnke, K. Müller-Buschbaum, J. Janek, *Batteries Supercaps* **2022**, *5*, 202200318.
[48] Z. Zhao-Karger, R. Liu, W. Dai, Z. Li, T. Diemant, B. P. Vinayan, C. Bonatto Minella, X. Yu, A. Manthiram, R. J. Behm, M. Ruben, M. Fichtner, *ACS Energy Lett.* **2018**, *3*, 2005.
[49] A. Jain, S. P. Ong, G. Hautier, W. Chen, W. D. Richards, S. Dacek, S. Cholia, D. Gunter, D. Skinner, G. Ceder, K. A Persson, *APL Mater.* **2013**, *1*, 11002.
[50] W. Zhang, D. A. Weber, H. Weigand, T. Arlt, I. Manke, D. Schröder, R. Koerver, T. Leichtweiss, P. Hartmann, W. G. Zeier, J. Janek, *ACS Appl. Mater. Interfaces* **2017**, *9*, 17835.
[51] a) P. Hohenberg, W. Kohn, *Phys. Rev.* **1964**, *136*, B864; b) W. Kohn, L. J. Sham, *Phys. Rev.* **1965**, *140*, A1133.
[52] P. E. Blöchl, *Phys. Rev. B* **1994**, *50*, 17953.
[53] J. Sun, A. Ruzsinszky, J. P. Perdew, *Phys. Rev. Lett.* **2015**, *115*, 36402.
[54] a) G. Kresse, J. Furthmüller, *Phys. Rev. B* **1996**, *54*, 11169; b) G. Kresse, J. Hafner, *Phys. Rev. B* **1993**, *47*, 558; c) G. Kresse, D. Joubert, *Phys. Rev. B* **1999**, *59*, 1758.
[55] D. Sheppard, R. Terrell, G. Henkelman, *J. Chem. Phys.* **2008**, *128*, 134106.

© 2024 The Authors. Advanced Energy Materials published by Wiley-VCH GmbH

16146840, 0, Downloaded from https://onlinelibrary.wiley.com/doi/10.1002/aenm.202402269 by Karlsruher Institut F., Wiley Online Library on [16/09/2024]. See the Terms and Conditions (https://onlinelibrary.wiley.com/terms-and-conditions) on Wiley Online Library for rules of use; OA articles are governed by the applicable Creative Commons License